Real-time, high-resolution study of nanocrystallization and fatigue cracking in a cyclically strained metallic glass

Cheng-Cai Wang[a,1], Yun-Wei Mao[a,1], Zhi-Wei Shan[a,2], Ming Dao[b,2], Ju Li[a,b,c], Jun Sun[a], Evan Ma[a,d], and Subra Suresh[e,2]

[a]Center for Advancing Materials Performance from the Nanoscale and Hysitron Applied Research Center in China, State Key Laboratory for Mechanical Behavior of Materials, Xi'an Jiaotong University, Xi'an 710049, People's Republic of China; Departments of [b]Materials Science and Engineering and [c]Nuclear Science and Engineering, Massachusetts Institute of Technology, Cambridge, MA 02139; [d]Department of Materials Science and Engineering, Johns Hopkins University, Baltimore, MD 21218; and [e]Department of Materials Science and Engineering, Carnegie Mellon University, Pittsburgh, PA 15213

Contributed by Subra Suresh, October 30, 2013 (sent for review September 22, 2013)

Metallic glasses (MGs) exhibit greater elastic limit and stronger resistance to plastic deformation than their crystalline metal counterparts. Their capacity to withstand plastic straining is further enhanced at submicrometer length scales. For a range of microelectromechanical applications, the resistance of MGs to damage and cracking from thermal and mechanical stress or strain cycling under partial or complete constraint is of considerable scientific and technological interest. However, to our knowledge, no real-time, high-resolution transmission electron microscopy observations are available of crystallization, damage, and failure from the controlled imposition of cyclic strains or displacements in any metallic glass. Here we present the results of a unique in situ study, inside a high-resolution transmission electron microscope, of glass-to-crystal formation and fatigue of an Al-based MG. We demonstrate that cyclic straining progressively leads to nanoscale surface roughening in the highly deformed region of the starter notch, causing crack nucleation and formation of nanocrystals. The growth of these nanograins during cyclic straining impedes subsequent crack growth by bridging the crack. In distinct contrast to this fatigue behavior, only distributed nucleation of smaller nanocrystals is observed with no surface roughening under monotonic deformation. We further show through molecular dynamics simulation that these findings can be rationalized by the accumulation of strain-induced nonaffine atomic rearrangements that effectively enhances diffusion through random walk during repeated strain cycling. The present results thus provide unique insights into fundamental mechanisms of fatigue of MGs that would help shape strategies for material design and engineering applications.

fatigue crack initiation | fatigue crack growth | fracture | shear diffusion transformation zone

Metallic glasses (MGs) possess several unique physical properties, including greater elastic limit and stronger resistance to plastic deformation, compared with crystalline metals and alloys (1–7). For a range of microelectromechanical applications (1, 7–12), the damage tolerance and crack resistance of MGs from thermal and mechanical stress or strain cycling under partial or complete constraint is of significant scientific and technological interest (13–18). Bulk MGs can undergo fully reversible elastic deformation to a strain limit of about 2%, more than an order of magnitude greater than that of coarse-grained crystalline metals, whereupon inelastic deformation commences at stress levels on the order of gigapascals (1, 2). Such high strength, however, is often accompanied by very limited ductility at room temperature. Experiments on MGs in thin-film form or as small-volume structures (typically hundreds of nanometers in linear dimensions) reveal that their elastic strain limit and corresponding strength are further enhanced, to values double those of bulk MGs (7–9). These findings suggest opportunities to use MGs in micro- and nanoscale systems and flexible electronic devices. Such applications, in addition to those in traditional structural components, also inevitably involve service conditions that introduce cyclic variations in thermal stresses and mechanical vibrations, as well as fully or partially constrained deformation. Consequently, the resistance of MGs to the onset and progression of deformation, damage, and cracking under cyclic straining is a topic of research and practical interest (15–22). Despite this need, the fatigue characteristics and mechanisms of MGs are not well understood, and to our knowledge no studies have been performed to date to document real-time, high-resolution observations of cyclic deformation and failure mechanisms of any MG inside a TEM.

Results and Discussion

In this work, microbeams of an $Al_{88}Fe_7Gd_5$ MG were fabricated through focused ion beam (FIB) machining from a melt-spun ribbon. This microfabrication process introduced a starter notch in the MG test specimen (Fig. 1*A*) so that fatigue damage and cracking occur within the field of view in the transmission electron microscope (TEM). Fig. 1*B* is a scanning electron microscope (SEM) image of an actual test specimen (with a total microbeam length of 3,300 nm, a middle section width of 800 nm, a middle section thickness of ~100 nm, and an initial notch length of ~220 nm). Cyclic deformation was applied in situ through a Hysitron PI95 deformation device inside a TEM

Significance

The formation of nanocrystals and cracks in metallic glasses subjected to cyclically varying strains in micro- and nanoscale systems is a topic of scientific and technological interest. However, no real-time studies of such phenomena in fatigued metallic glasses have thus far been reported. Here we present unique observations of nanocrystallization and the onset and progression of fatigue failure in a metallic glass through cyclic straining experiments conducted inside a high-resolution transmission electron microscope. Molecular dynamics simulations were also performed to elucidate the underlying mechanisms. We expect that these techniques and results will provide unique fundamental insights into how crystallization occurs in a wide variety of amorphous materials and will help develop strategies for the design and use of metallic glasses.

Author contributions: C.-C.W., Y.-W.M., Z.-W.S., M.D., J.L., J.S., E.M., and S.S. designed research; C.-C.W. and Y.-W.M. performed research; Z.-W.S., M.D., J.L., J.S., E.M., and S.S. contributed new reagents/analytic tools; C.-C.W., Y.-W.M., Z.-W.S., M.D., J.L., E.M., and S.S. analyzed data; and C.-C.W., Y.-W.M., Z.-W.S., M.D., J.L., E.M., and S.S. wrote the paper.

The authors declare no conflict of interest.

Freely available online through the PNAS open access option.

[1]C.-C.W. and Y.-W.M. contributed equally to this work.

[2]To whom correspondence may be addressed. E-mail: suresh@cmu.edu, zwshan@mail.xjtu.edu.cn, or mingdao@MIT.EDU.

This article contains supporting information online at www.pnas.org/lookup/suppl/doi:10.1073/pnas.1320235110/-/DCSupplemental.

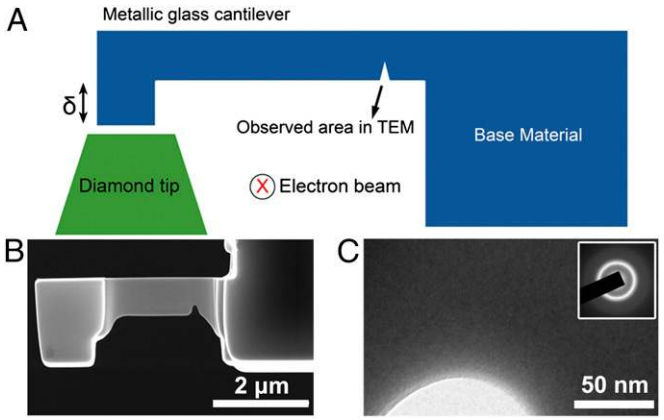

Fig. 1. In situ fatigue testing of the metallic glass inside a TEM. (*A*) Schematic of the experimental setup. Note that the electron beam direction is perpendicular to the plane. (*B*) SEM image showing a sample fabricated by a FIB. (*C*) Bright-field TEM image of the notch tip before testing shows that the sample has a fully amorphous structure, as evidenced by the SADP (*Inset*).

(JEM-2100F; JEOL). Because typical deformation conditions potentially imposed on MGs in microsystems are likely to be displacement/strain controlled rather than stress controlled, cyclic straining was applied under a displacement-controlled mode. Our ability to impose fixed values of cyclic displacements δ (indicated in Fig. 1*A*) in a well-controlled manner using the in situ deformation stage inside the high-resolution TEM enables us to establish quantitative and mechanistic relationships among microstructure, mechanical deformation, onset, and progression of damage and failure at the atomic scale (5). The imposed displacement was controlled between a minimum value of 160 nm and a maximum value of 400 nm at a constant cyclic frequency of 1 Hz (triangular waveform), and the corresponding strain range was between 0.8% and 2.1%. Fig. 1*C* is a TEM image of the semicircular notch-tip region where the tip radius is about 25 nm. Selected area diffraction patterns (SADP) of this as-fabricated, untested notch-tip region (Fig. 1*C*, *Inset*) confirm a fully amorphous atomic structure.

Fig. 2*A* compares three high-magnification images of the notch-tip region for the untested, cyclically strained, and monotonically strained specimens. Before any mechanical loading, the as-fabricated specimen shown in Fig. 2*A*, *Left* reveals a notch-tip region that is "smooth" at the scale of observation. Fig. 2*A*, *Center* shows that repeated notch-tip straining caused by 490 displacement cycles results in the "roughening" of the surface of the notch at the nanometer scale. This behavior is analogous to the process of surface roughening introduced by the irreversibility of cyclic slip in crystalline metals whereby initially smooth surfaces of the specimen form "intrusions" and "extrusions", providing sites for fatigue crack nucleation (23). However, the corresponding SADP found no signs of crystallization as of 490 cycles. If the specimen was subjected to monotonic loading with a maximum strain of ~12%, no obvious surface roughening was visible at the free surface of the notch (Fig. 2*A*, *Right*) or even in the vicinity of a shear band that emanated from the surface under intense strain localization (Fig. S1). It is thus seen from the three images in Fig. 2*A* that repeated cyclic loading leads to surface damage in the form of atomic scale roughening after several hundred cycles.

Fig. 2*B* is a collection of three bright-field TEM images of the notch-tip region after 980, 1,470 and 1,960 cycles, respectively. These images, along with *SI Text*, reveal the following mechanistic processes. Local cyclic deformation at the roughened surface of the notch tip leads to the initiation of a fatigue crack. Many tiny nanograins are nucleated in this highly strained region. High-resolution video photography of the crack tip shows the growth of a single nanocrystal at the fatigue crack tip with an increasing number of fatigue cycles (Movie S1). By the end of 1,960 cycles, the nanocrystal had grown to a diameter of ~27 nm. Fig. 2*B*, *Right Inset* shows the SADP taken from the corresponding crack-tip area that confirmed the existence of the "giant" grain as well as a few satellite grains in the surrounding amorphous matrix. The grain size and its distribution resulting from cyclic straining are very different from those from monotonic loading (24–27) with similar test geometry. The nanograins formed by monotonic loading are localized in the shear band ahead of the notch and had a grain size of only a few nanometers (for example, Fig. S2). To assess how thermally induced nanocrystallization differs from that mechanically induced by monotonic or cyclic straining, we performed additional experiments. Thermal treatment of an Al-based MG ribbon (heated to 150 °C for about 20 min in the air) produces nanograins of approximately equal size over the entire specimen as shown in Fig. S3. Fig. S3 also indicates that all of the nanocrystals have a face-centered cubic structure irrespective of whether they were induced thermally or by monotonic or cyclic mechanical deformation.

The process of nanocrystal formation and growth is further elucidated by the three high-resolution TEM images in Fig. 2*C*. Fig. 2*C*, *Left* and *Center* represents the crystalline structure within the amorphous metal matrix after 1,470 and 1,960 displacement cycles, respectively. Fig. 2*C*, *Left* and *Center* shows a larger grain (G_1) neighboring a smaller grain (G_2); Fig. 2*C*, *Left Inset* is based on a fast Fourier transformation (FFT) analysis of an area that contains both G_1 and G_2, with the orientation mismatch between the grains being ~15°. This was also confirmed by measuring the lattice fringe in a magnified view. After being subjected to an additional 490 cycles, G_1 grew further by consuming G_2, as was supported by the FFT image (Fig. 2*C*, *Center Inset*) as well as by the corresponding inverse FFT image (Fig. 2*C*, *Right*), which revealed that the large grain contained several dislocations.

Having established through real-time, high-resolution TEM that cyclic deformation at room temperature leads to nanocrystal formation and growth in the MG, we now show quantitatively how this structure evolution influences the rate of fatigue crack growth (see *SI Text, Estimation of Crack Length* and Figs. S4–S7 for the definition of crack length). Consider first the variation of the maximum and minimum load during the first 490 fatigue cycles imposed under displacement amplitude control. At the beginning of fatigue loading, the load amplitude corresponding to the fixed displacement amplitude is relatively constant for about 350 cycles, because local cyclic straining produces primarily elastic deformation (Fig. 3*A*). The initiation of nanoscale roughening of the free surface of the notch tip (as was seen in Fig. 2*A*, *Center*), between cycle numbers 350 and 490, appears to have facilitated the onset of inelastic deformation, as supported by the sample edge roughening shown in Fig. 2*A*, *Center*. A crack was observed to nucleate at the beginning of the second set of the cyclic loading tests at around 500 cycles. Fig. 3*C* is a plot of the fatigue crack length, defined as the distance between the advancing tip and the original edge surface position, as a function of the number of cycles, beginning with cycle no. 500. For the subsequent 300 cycles, the crack length increased with fatigue loading. The intense local straining ahead of the advancing sharp fatigue crack, however, leads to a zone of nanocrystals, typically several nanometers in diameter. The coalescence of these nanocrystals (as indicated by the images shown in Fig. 2 *B* and *C*), however, produces a large grain that impedes further crack advance. Nanograin growth influences the rate of fatigue crack growth in several distinct and measurable ways. First, with the growth of several nanograins, crack length begins to decrease (between cycle nos. 800 and 980 in Fig. 3*C*) with an increase in the number of cycles as the presence of a large grain "shields" the crack tip from the severity of cyclic straining. Once the crack

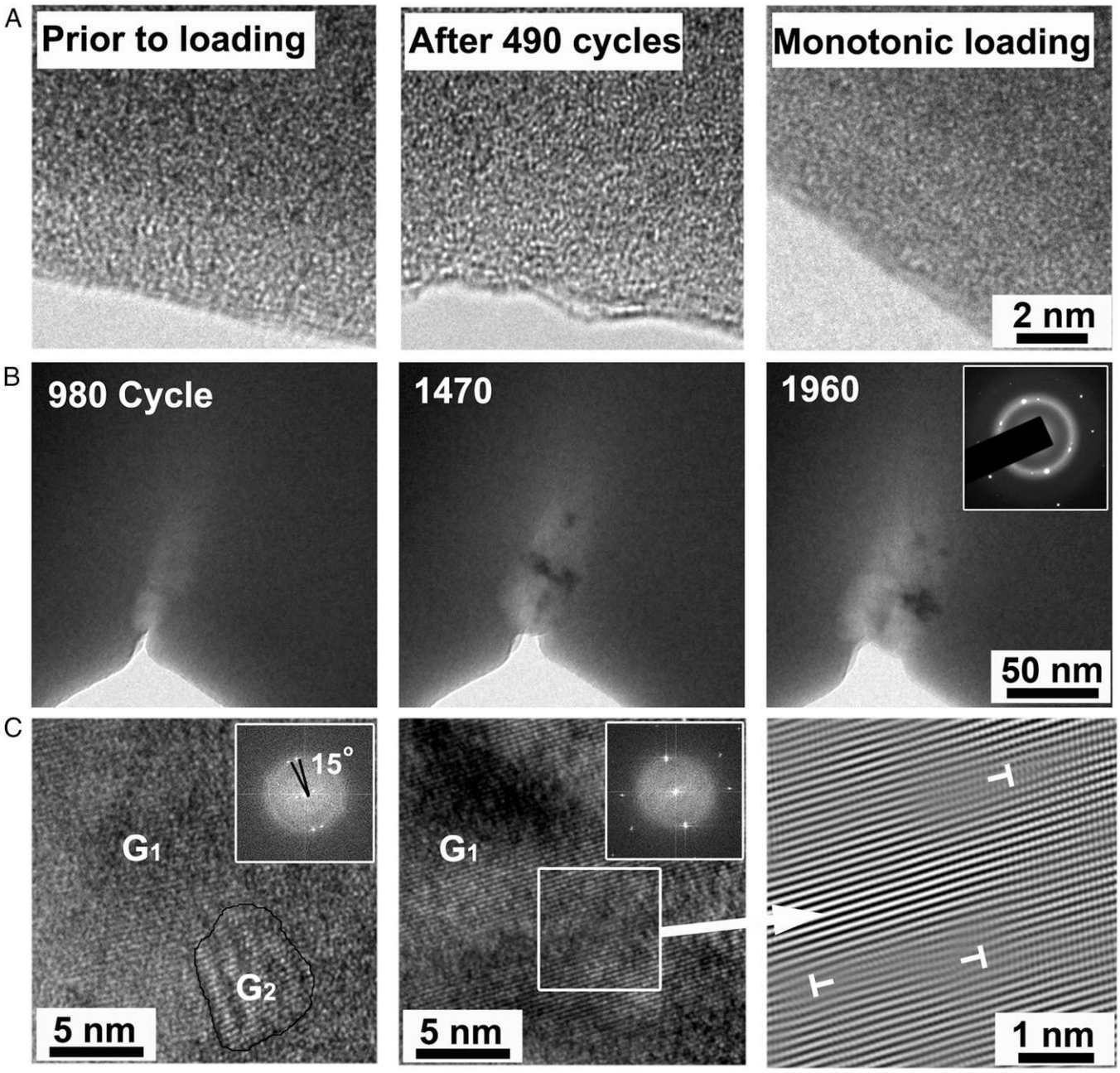

Fig. 2. Microstructure evolution of $Al_{88}Fe_7Gd_5$ metallic glass in response to cyclic straining. (*A*) High-magnification images of the notch-tip region for the untested, cyclically strained (maximum strain ~2.1%), and monotonically strained (maximum strain >10%) specimens. (*B*) Fatigue crack morphology after 980, 1,470, and 1,960 cycles, respectively. SADP (*Inset*) demonstrated the existence of crystalline phase ahead of the crack tip. Note grain growth and crack-tip blunting with cyclic straining. (*C*) High-resolution TEM observation of two grains (G_1 and G_2) ahead of the crack tip (*Left*) and their coalescence after 490 additional cycles (*Center*). FFT (*Left Inset*) suggested the initial angle between the two grains was ~15°. Inverse FFT (*Right*) of the part framed by the solid white box (*Center*) revealed that the final "giant" grain contained several dislocations, indicated by the white symbols (*Right*).

tip "breaks free" from the influence of this shielding grain, an abrupt increase in crack length occurs due to a burst of crack growth. However, as the surrounding nanocrystals ahead of this advancing crack front grow further, the apparent crack length decreases once again because of the shielding effect (region between cycle nos. 1,000 and 1,200 in Fig. 3*C*). This shielding effect is clearly manifested as a distinct load drop between cycle nos. 1,000 and 1,200 in Fig. 3*B*. Fig. 3*B* also shows a transition from tension–tension to tension–compression fatigue load, i.e., starting from cycle no. ~1,050, as a consequence of plastic deformation. The concurrent mechanisms of damage evolution at the crack tip, nanocrystallization, and grain growth thus lead to the anomalous crack growth response shown in Fig. 3*C*. Another consequence of this anomalous fatigue behavior is the blunting of the crack tip with cyclic loading and grain growth (Fig. 2*B*).

Temperature-driven structural disorder-to-order transitions such as the nucleation of crystals in liquid upon cooling have been extensively studied (28–30). However, stress-driven disorder-to-order transitions, such as the one described in this work, are seldom investigated (24, 25). In contrast to scalar temperature, tensorial stress stimuli for crystallization should lead to a preferred texture/directionality. Indeed, our molecular dynamics

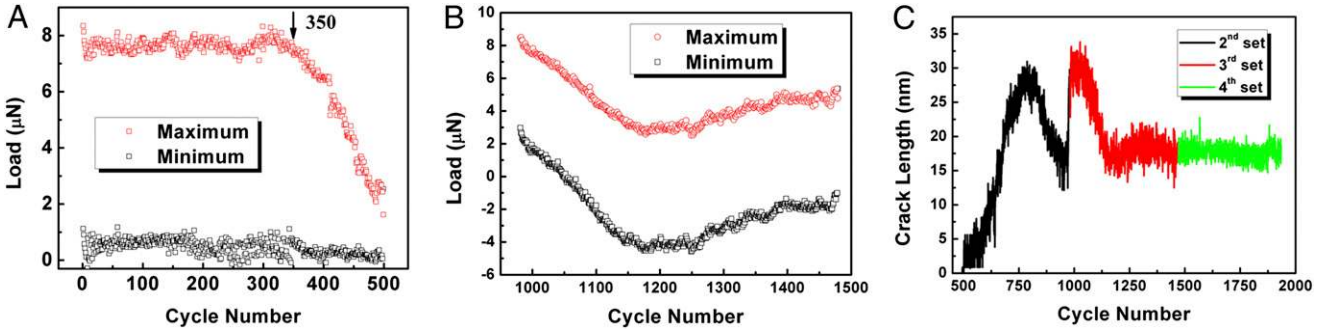

Fig. 3. Maximum/minimum loads under a fixed value of imposed displacement amplitude and crack length evolution as a function of fatigue cycles. (*A*) Load vs. cycle number for the first set of tests spanning 490 cycles. (*B*) Load vs. cycle number for the third set from 981 to 1,470 cycles. (*C*) Crack length evolution with increasing cycle number.

simulations below show that the nucleated nanocrystals tend to have their crystallographic slip planes parallel to the local shear stress direction. Irrespective of stimulation by temperature or stress, going from structural disorder to order requires "diffusive" reshuffling of atoms. Although the ability of MG to plastically deform under stress by shear transformation zones (STZs) is well known (2, 11), a key question here is how stress enhances "atomic diffusivity" in MG. Prior work (24) on room temperature nanocrystallization during the nanoindentation of a bulk metallic glass also pointed to the possibility of such enhanced atomic diffusivity from severe local stress and flow-induced dilation. To quantify and understand the atomic structure evolution, we carried out molecular dynamics (MD) simulations of cyclic-stress–induced glass–crystal transition. We considered a binary MG $Al_{50}Fe_{50}$, which shows structure evolution and plastic deformation behavior similar to the MG studied in cyclic loading experiments (details of atomistic simulation can be found in *SI Text, Molecular Dynamics Simulation*).

The evolution of atomic geometries is analyzed by the following "deformation–diffusion" decomposition (31, 32),

$$\mathbf{d}_{ji} = \mathbf{d}_{ji}^{0}\mathbf{J}_i + \mathbf{s}_{ji}, \quad j \in N_i, \qquad [1]$$

where i is the atom being analyzed, $j \in N_i$ are i's original neighbors (defined within some cutoff radius) in a reference configuration, $\mathbf{d}_{ji}^{0}$ is the original distance between atoms j and i in the reference configuration, and $\mathbf{d}_{ji}$ is their current distance vector. The first term in [**1**] reflects local deformation (shape change), whereas the second term reflects additional atomic movements or shuffling beyond mere shape change. The extent of local diffusion is defined by

$$D_i^2 \equiv \frac{1}{N_i}\sum_{j\in N_i}\left|\mathbf{s}_{ji}\right|^2 = \frac{1}{N_i}\min_{\mathbf{J}_i}\sum_{j\in N_i}\left|\mathbf{d}_{ji}^{0}\mathbf{J}_i - \mathbf{d}_{ji}\right|^2, \qquad [2]$$

where the 3 × 3 local deformation gradient $\mathbf{J}_i$ needs to be numerically optimized to minimize D_i^2. Although D_i^2 might be small, it accumulates during repeated cyclic mechanical deformation. Fig. 4*A* shows the atomic configuration of the notch area after 275 cycles of strain (see Fig. S8*A* for the details of the MD simulation setup): The long-range periodic packing of atoms clearly corresponds to crystallization in the active zone. Statistics of the atomistic D_i^2 after different cycles are plotted in Fig. 4*C*. The variation of atom fraction vs. D_i^2 for the first half cycle (representing monotonic loading) showed a sharp decrease. Then it gradually increased to reach a peak value at large diffusional displacement (D_i^2) as the cycle number increased; e.g., the corresponding D_i^2 equaled 5.8 Å^2 for the peak after 275 cycles (Fig. S8*A*). Although the peak D_i^2 becomes sharper with increasing numbers of cycles, it occurs at an approximately constant square displacement value of about $D_C^2 = 5.5$ Å^2, which characterizes the initiation of crystallization. The root mean square value of this critical threshold, $\sqrt{D_C^2} = 2.3$ Å, can be regarded as an upper bound to the minimal "glass-to-crystal" distance d_C, defined to be the minimal nonaffine displacement per atom necessary to reorder a disordered system, akin to the least number of steps to solve a Rubik's Cube. The smallness of d_C bounded by our simulation trajectories indicates that the glass configurations studied here are not too "far" from their nearest crystal configuration, at least for binary glasses. However, at low temperature T and zero external stress $\sigma_{ext} = 0$, the energy barriers Q are still too high despite the short distance in phase space (33) on the potential energy landscape; thus only when σ_{ext} is high enough can sufficient atomic shuffling occur, along with local and global shape changes. Our MD trajectories confirm that stress drives both plasticity (shear transformation zone) and diffusion ("diffusion transformation zone") in metallic glass, the rate of which may be modeled by a generic transition-state theory expression

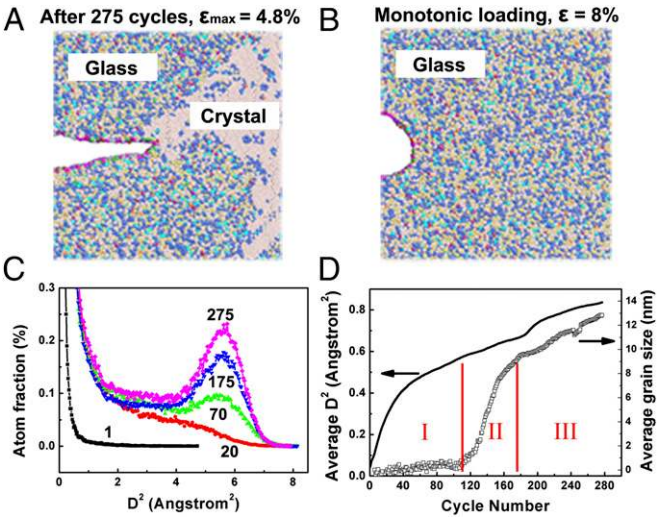

Fig. 4. MD simulation on fatigue tests of Al-Fe metallic glass. Two identical specimens were tested under cyclic straining (between strain limits of 3 ± 1.8%) and monotonic loading (strained to 8%). (*A*) The crystalline phase can be seen clearly after 275 cycles. (*B*) The sample remained amorphous under monotonic loading even though the strain reached 8%. (*C*) The distribution of the atom fraction vs. the square of nanoaffine displacement (D^2) for cycle nos. 1, 20, 70, 175, and 275. (*D*) Both the averaged D^2 (solid black line) and the average grain size (curve with circles) increased with increasing cycle number.

$$\propto \exp\left(-\frac{Q_m(\sigma_{\text{ext}}, v)}{k_B T}\right), \quad [3]$$

where $Q_m = Q_m(\sigma_{\text{ext}}, v)$ is a microscopic activation barrier; v is the "free volume", an internal state variable that could change after each event; and m is the event menu option (see figure 1 of ref. 34 for illustration). The shear transformation zone thus can also possess a dual character of diffusion and may be called a "shear diffusion transformation zone" (SDTZ). Note that in [**3**], stress has both indirect and direct effects on the rate of diffusion. The indirect effects come from a change of v after stress-driven flow [rejuvenation (34, 35) or flow-induced dilation (24)] and later even a possible change of T (32). However, there is a direct effect of stress on diffusion also, as represented by the first dependency of $Q_m(\sigma_{\text{ext}}, v)$. In [**3**], increasing σ_{ext}, increasing v, or increasing T all should lead to an accelerated rate of diffusion in metallic glass, but the functional dependencies on $\sigma_{\text{ext}}, v, T$ are generally not the same due to inequivalent positions in the fraction $\frac{Q_m(\sigma_{\text{ext}}, v)}{k_B T}$.

The averaged $\overline{D^2}$ showed a nonlinear increase with increasing strain cycles (Fig. 4*D*, black solid line). Correspondingly, the average grain size ($d \equiv \sqrt{A}$), where A is the grain area, can be classified into three regimes according to the cycle number. For regime I (cycles ranging from 1 to ~110), the average grain size remains subnanometer (Fig. 4*D*, curve with circles). For regime II (cycles ranging from 110 to ~175), rapid grain growth sets in suddenly following the incubation period in regime I. After the cycle number exceeds 175 (in regime III), the grain growth rate decreases significantly.

For comparison, atomistic simulation of monotonic deformation (imposed strain ~8%) of the same sample geometry is shown in Fig. 4*B* (also Fig. S8*B*). The active zone was along the plane with maximum shear stress. Neither obvious localization nor long-period packing of atoms (of glassy structure) was observed in these zones (e.g., Fig. 4*B*). This is further supported by the observation that the fraction of atoms with larger nonaffine displacement remains quite low. We compute a "diffusion-to-shear ratio" $\overline{D^2}/\overline{J_2}$, where $\overline{J_2}$ is the mean Mises shear strain invariant from $\mathbf{J}_i$, to quantify the relative diffusive to displacive nature of the structural transformation, based on atomic trajectories. From our simulations, monotonic loading beyond global yielding gives a lower $\overline{D^2}/\overline{J_2}$ than subyielding cyclic loading. Furthermore, $\overline{D^2}/\overline{J_2}$ increases with cycle number, due to the cumulative nature of random atomic shuffling displacements that occur by random walk. So it is easier to observe crystallization in small-scale simulations by cyclic deformation than by monotonic deformation. We note that crystallization is still observed experimentally in monotonic loading (24), but the local strains in the shear bands observed in the experimental samples are much larger than what can be easily achieved in simulations. These shear bands cause flow dilatation (24, 36, 37) that triggers more nucleation of nanocrystals inside a mature shear band. In contrast, the relatively lower stress (below the yielding point) under cyclic loading was not high enough to generate a shear band in one cycle. Instead, local accumulation of nonaffine displacements (Fig. S8*A*) continues with an increase in strain cycles culminating in an amorphous to crystal transition (Fig. 2). It is worth noting that crystallization in our experiments and simulations is a mechanical deformation-driven process without obvious temperature rise, consistent with previous studies (24) of nanocrystal formation at room temperature in a metallic glass subject to nanoindentation.

The simulated snapshots of the evolution of atomistic configuration in the MG are shown in Fig. S9. Our simulations show that the nucleated crystals tend to have their crystallographic slip or close-packed plane parallel to the local shear stress direction at the nucleation site. Only atoms with coordinate number (CN) ~14 (the number of atoms perceived as neighbors in the body centered cubic (bcc) crystal that formed in the $Al_{50}Fe_{50}$ simulation model) are displayed. After 110 cycles, some atoms with CN ~14 aggregated into a cluster (nanocrystal) on the right side ahead of the propagating crack, and this crystal grew rapidly until it reached the fatigue crack tip. The crystal was not very stable at the beginning and broke up into several pieces during the unloading. Along with increasing strain cycles, the central nucleus gradually became larger and more stable such that its "transient" aggregation with some other tiny clusters became a more permanent structure (Movie S2). The scenario agrees well with the experimental observations depicted in Fig. 2*B*. The corresponding cyclic load and crack length evolution from MD simulation (Fig. S9 *B* and *C*) showed trends similar to those observed in the experiments (Fig. 3 *B* and *C*), where a switch from local tension–tension to tension–compression fatigue was noted as a consequence of the shielding of the crack and the attendant retardation of crack growth by nanograin formation and growth.

The abnormal fatigue crack propagation behavior in nanoscale $Al_{88}Fe_7Gd_5$ MG could be attributed to several factors. First, from the viewpoint of energy, repeated straining causes sufficient $\overline{D^2}$ to induce the glass-to-crystal transition near the fatigue crack tip, which dissipates mechanical energy, thereby reducing the effective driving force for crack propagation. Second, MGs at the submicron scale exhibit higher plastic flow stress and more distributed shear transformations than their bulk counterparts (4, 5, 11). Third, for small-volume samples, the phase transition ahead of the fatigue crack could achieve much higher efficiencies (because of a higher concentration of the number of nanocrystals per unit volume) to improve the fatigue tolerance, compared with that in bulk samples. Fourth, cyclic straining-induced crystalline phases near the fatigue crack tip, in conjunction with a plasticity-induced tension-compression fatigue load with displacement-controlled straining, would bridge the wakes of crack and thus extrinsically enhance the fatigue tolerance (38). This is evidenced by the unexpected increase of maximum load in Fig. 3 and by the heavy plastic deformation experienced in the crystalline phase in Fig. 2 (with dislocations inside crystals, as seen in Fig. 2*C*). In addition, the volume shrinkage [MGs are slightly less dense than their crystalline counterparts (2, 39)] during glass-to-crystal transition might induce additional (residual) compressive stress in the surrounding MG matrix (40), which favors crystallization and grain growth processes in MGs (25, 39). In other words, the fatigue tolerance of the MG beam is self-improved in situ with strain cycles.

Conclusion

In summary, glass-to-crystal transition induced by cyclic straining has been demonstrated using quantitative in situ fatigue tests performed on an Al-based MG inside a TEM. It is shown that cyclic straining leads to the nanoscale roughening of an initially smooth surface in the metallic glass. This process is mechanistically analogous to the roughening of surfaces of metallic crystals due to fatigue whereby intrusions and extrusions are created at surfaces, providing preferential sites of stress concentration for fatigue crack nucleation. Such surface roughening is visibly absent if the MG is instead subjected to monotonic straining even to much higher plastic deformation levels. Nanocrystals nucleate around zones of intense deformation produced by mechanical straining. Under cyclic straining, nanocrystals coalesce and grow to average dimensions several times larger than those seen under monotonic straining. Molecular dynamics simulations provide a clear mechanistic basis for these experimentally observed processes. The simulations reveal that the accumulation of local nonaffine displacements, facilitated by stress and assisted by the excess volume that is continuously generated within the

shear transformation zones of the MG, leads to the formation and growth of nanocrystals. Our MD results show that the mean square displacement, $\overline{D^2}$, which is a measure of the extent of the local atomic shuffling needed to achieve a disorder-to-order transition, accumulates with stress cycles. This stress-assisted "effective diffusion" with enhanced "atomic random walk" by SDTZ events resembles the high atomic mobility at elevated temperatures and rationalizes why cyclic straining leads to nanocrystallization at room temperature. The formation of nanograins, which grow to average diameters as large as about 27 nm, causes shielding of the fatigue crack by reducing the effective driving force for crack growth and resisting crack propagation. These results documenting real-time and high-resolution mechanical response provide fundamental insights into the atomic-level mechanisms governing fatigue and crystallization of metallic glasses.

Methods

The submicron-sized cantilever beams were fabricated using a FIB (Helios NanoLab600i) from $Al_{88}Fe_7Gd_5$ metallic glass ribbons produced by melt spinning. In situ mechanical testing was conducted inside a JEM-2100F TEM (JEOL) equipped with two CCD cameras, i.e., Model 830 and ORIUS SC200 (Gatan), using a PI95 TEM PicoIndenter (Hysitron) with a time and displacement resolution of ~0.4 μN and ~1 nm, respectively. Both the cyclic and the monotonic loading tests were conducted in displacement-control mode, which is more sensitive to transient structure evolution. Fig. S10 shows a typical cyclic displacement loading function with a triangular waveform and a frequency 1 Hz; an initial displacement of 400 nm (~50% of the middle section sample width) was applied from the initial zero-force configuration followed by cyclic displacements between 400 nm and 150 nm. To obtain detailed structure information (diffraction pattern and high-quality images), the fatigue experiment was terminated after each 490 cycles to perform high-resolution imaging. After the high-resolution image was obtained, another set of fatigue testing was started again on the same specimen with the same displacement-controlled amplitude, while taking the previously unloaded configuration as the reference zero displacement position. Four samples have been cyclically tested and more than 10 samples have been monotonically tested closely under identical conditions. All results shown in this work were repeatable. Details of molecular dynamics simulation are given in *SI Text*.

ACKNOWLEDGMENTS. This work was supported by the Natural Science Foundation of China under the following Grants: 50925104, 51231005, 51321003, the 973 Programs of China (2010CB631003 and 2012CB619402), and the 111 Project of China (B06025). J.L. acknowledges support by the US National Science Foundation (NSF) under Grants NSF DMR-1240933 and DMR-1120901, and E.M. acknowledges support from the NSF under Grant NSF-DMR-0904188. M.D. and S.S. acknowledge support from the Singapore–Massachusetts Institute of Technology Alliance (SMA).

1. Greer AL, Ma E (2007) Bulk metallic glasses: At the cutting edge of metals research. *MRS Bull* 32(8):611–615.
2. Schuh CA, Hufnagel TC, Ramamurty U (2007) Overview No.144 - Mechanical behavior of amorphous alloys. *Acta Mater* 55(12):4067–4109.
3. Wang WH, Dong C, Shek CH (2004) Bulk metallic glasses. *Mater Sci Eng Rep* 44(2–3): 45–89.
4. Guo H, et al. (2007) Tensile ductility and necking of metallic glass. *Nat Mater* 6(10): 735–739.
5. Shan ZW, et al. (2008) Plastic flow and failure resistance of metallic glass: Insight from in situ compression of nanopillars. *Phys Rev B* 77(15):155419.
6. Chen CQ, Pei YT, De Hosson JTM (2010) Effects of size on the mechanical response of metallic glasses investigated through in situ TEM bending and compression experiments. *Acta Mater* 58(1):189–200.
7. Jang D, Greer JR (2010) Transition from a strong-yet-brittle to a stronger-and-ductile state by size reduction of metallic glasses. *Nat Mater* 9(3):215–219.
8. Tian L, et al. (2012) Approaching the ideal elastic limit of metallic glasses. *Nat Commun* 3:609.
9. Wang CC, et al. (2012) Sample size matters for Al88Fe7Gd5 metallic glass: Smaller is stronger. *Acta Mater* 60(13–14):5370–5379.
10. Kumar G, Desai A, Schroers J (2011) Bulk metallic glass: The smaller the better. *Adv Mater* 23(4):461–476.
11. Cheng YQ, Ma E (2011) Atomic-level structure and structure-property relationship in metallic glasses. *Prog Mater Sci* 56(4):379–473.
12. Greer JR, De Hosson JTM (2011) Plasticity in small-sized metallic systems: Intrinsic versus extrinsic size effect. *Prog Mater Sci* 56(6):654–724.
13. Wang GY, Liaw PK, Morrison ML (2009) Progress in studying the fatigue behavior of Zr-based bulk-metallic glasses and their composites. *Intermetallics* 17(8):579–590.
14. Wang GY, Liaw PK, Yokoyama Y, Inoue A, Liu CT (2008) Fatigue behavior of Zr-based bulk-metallic glasses. *Mater Sci Eng A Struct Mater Prop Microstruct Process* 494(1–2): 314–323.
15. Jang DC, Maass R, Wang GY, Liaw PK, Greer JR (2013) Fatigue deformation of microsized metallic glasses. *Scr Mater* 68(10):773–776.
16. Chuang C-P, et al. (2013) Fatigue-induced damage in zr-based bulk metallic glasses. *Sci Rep* 3:2578.
17. Gilbert CJ, Ritchie RO, Johnson WL (1997) Fracture toughness and fatigue-crack propagation in a Zr-Ti-Ni-Cu-Be bulk metallic glass. *Appl Phys Lett* 71(4):476–478.
18. Gilbert CJ, Schroeder V, Ritchie RO (1999) Mechanisms for fracture and fatigue-crack propagation in a bulk metallic glass. *Metall Mater Trans A Phys Metall Mater Sci* 30(7): 1739–1753.
19. Menzel BC, Dauskardt RH (2006) Stress-life fatigue behavior of a Zr-based bulk metallic glass. *Acta Mater* 54(4):935–943.
20. Hess PA, Menzel BC, Dauskardt RH (2006) Fatigue damage in bulk metallic glass II: Experiments. *Scr Mater* 54(3):355–361.
21. Wang GY, Liaw PK (2010) Bending-fatigue behavior of bulk metallic glasses and their composites. *JOM* 62(4):25–33.
22. Flores KM, Johnson WL, Dauskardt RH (2003) Fracture and fatigue behavior of a Zr-Ti-Nb ductile phase reinforced bulk metallic glass matrix composite. *Scr Mater* 49(12):1181–1187.
23. Suresh S (1998) *Fatigue of Materials* (Cambridge Univ Press, Cambridge, UK).
24. Kim JJ, Choi Y, Suresh S, Argon AS (2002) Nanocrystallization during nanoindentation of a bulk amorphous metal alloy at room temperature. *Science* 295(5555):654–657.
25. Jiang WH, Atzmon M (2003) The effect of compression and tension on shear-band structure and nanocrystallization in amorphous Al90Fe5Gd5: A high-resolution transmission electron microscopy study. *Acta Mater* 51(14):4095–4105.
26. Chen MW, Inoue A, Zhang W, Sakurai T (2006) Extraordinary plasticity of ductile bulk metallic glasses. *Phys Rev Lett* 96(24):245502.
27. Yavari AR, et al. (2012) Crystallization during bending of a Pd-based metallic glass detected by x-ray microscopy. *Phys Rev Lett* 109(8):085501.
28. Turnbull D (1950) Formation of crystal nuclei in liquid metals. *J Appl Phys* 21(10): 1022–1028.
29. Debenedetti PG (1996) *Metastable Liquids: Concepts and Principles* (Princeton Univ Press, Princeton).
30. Kawasaki T, Tanaka H (2010) Formation of a crystal nucleus from liquid. *Proc Natl Acad Sci USA* 107(32):14036–14041.
31. Falk ML, Langer JS (1998) Dynamics of viscoplastic deformation in amorphous solids. *Phys Rev E Stat Phys Plasmas Fluids Relat Interdiscip Topics* 57(6):7192–7205.
32. Shimizu F, Ogata S, Li J (2007) Theory of shear banding in metallic glasses and molecular dynamics calculations. *Mater Trans* 48(11):2923–2927.
33. Zhu T, Li J, Lin X, Yip S (2005) Stress-dependent molecular pathways of silica-water reaction. *J Mech Phys Solids* 53(7):1597–1623.
34. Zhao PY, Li J, Wang YZ (2013) Heterogeneously randomized STZ model of metallic glasses: Softening and extreme value statistics during deformation. *Int J Plast* 40:1–22.
35. Shimizu F, Ogata S, Li J (2006) Yield point of metallic glass. *Acta Mater* 54(16): 4293–4298.
36. Donovan PE, Stobbs WM (1981) The structure of shear bands in metallic glasses. *Acta Metall* 29(8):1419–1436.
37. Bokeloh J, Divinski SV, Reglitz G, Wilde G (2011) Tracer measurements of atomic diffusion inside shear bands of a bulk metallic glass. *Phys Rev Lett* 107(23):235503.
38. Ritchie RO (2011) The conflicts between strength and toughness. *Nat Mater* 10(11): 817–822.
39. Ye F, Lu K (1999) Pressure effect on crystallization kinetics of an Al-La-Ni amorphous alloy. *Acta Mater* 47(8):2449–2454.
40. Olsson M, Giannakopoulos AE, Suresh S (1995) Elastoplastic analysis of thermal cycling: Ceramic particles in a metallic matrix. *J Mech Phys Solids* 43(10):1639–1671.

Supporting Information

Wang et al. 10.1073/pnas.1320235110

SI Text

Estimation of Crack Length

We extract frames from our experimental movies and then use following image-processing method to characterize the crack length:

i) We decrease the bit depth of the original jpeg picture (e.g., Fig. S4*A*) to 8-bit (Fig. S4*B*) for further image processing.
ii) We use the Sobel method (the Sobel method is usually used on edge detection in image processing by computing an approximate gradient of the image intensity function) (1) to detect the boundary of the crack. Fig. S5 shows the resulting traced notch/crack boundary.
iii) Finding the apex of the crack (point A in Fig. S6) and the bottom of the notch profile (point B in Fig. S6), we draw a line between these two points.
iv) Detecting the reference point C in the notch/crack boundary and measuring the crack length. First, the vertical distance between the point on the curved edge line and the straight line AB is automatically measured, where the peak distance corresponds to the reference point C; second, the crack length of the fatigue crack was determined as the line distance AC as seen in Fig. S7; third, after rescaling the length AC to the scale bar, we get the real length of the crack.

Molecular Dynamics Simulation

To understand the structure evolution due to the cyclic straining, molecular dynamics (MD) simulation is used to reveal atomic rearrangement processes. Simulations on a binary bulk metallic glass (BMG) system ($Al_{50}Fe_{50}$) are performed in this study.

We adopt the Al-Fe interatomic potential of Mendelev et al. (2). The configuration is produced by adopting a similar procedure: (*i*) Glass samples consisting of 2,000 atoms are prepared from a melting-and-quenching simulation of a randomly substituted solid solution in a face centered cubic (fcc) lattice, whose temperature is raised gradually from 300 K to 3,000 K, equilibrated for 1,000 ps, and cooled down to 50 K, with the effective heating and cooling rates of 0.425 K/ps. The time step for integration is chosen to be 0.002 ps. Pressure is maintained at zero during both the heating and the cooling processes. The dimensions of as-prepared glass samples are ~$4 \times 4 \times 2$ nm. (*ii*) The final sample with dimension of ~$59 \times 74 \times 2$ nm is produced by multiplying the amorphous sample produced by step *i* along the *x* and *y* axes. (*iii*) A crack with a dimension of ~$22 \times 2 \times 2$ nm is created in the middle of the final sample. The ensemble used in the simulation is the isothermal–isobaric ensemble with conserved moles, pressure, and temperature (NPT). During simulations, cyclic loading is applied in the *y* direction with a strain rate of ~10^9/s whereas the strain rate in the *z* axis remains zero. The deformation is carried out under displacement-controlled mode and the strain range is set to be $3 \pm 1.8\%$ for cyclic testing. The set peak strain is close to the yield point from monotonic testing (~5.8%) such that we could monitor the structure changes and crack evolution within a reasonable time. In our adopted NPT ensemble, the temperature is strictly controlled around 50 K (only 0.1 K fluctuation is allowed). Thus, there is no temperature effect or any significant temperature rise in our simulations. On the other hand, the external stress would enhance the translational displacement of atoms in our simulated system, although it does not have a significant contribution to atoms' random vibration. Thus, the MD simulations suggest that the nanocrystallization can be induced by externally applied cyclic stress without temperature rise.

For comparison, we also performed a monotonic loading of the model with maximum strain up to 8%. The main results are shown in Fig. S8, using Falk and Langer's method (3). We also adopt the Honey–Anderson method to characterize the crystal (4, 5).

1. Heath M, Sarkar S, Sanocki T, Bowyer K (1998) Comparison of edge detectors. *Comput Vis Image Underst* 69(1):17–22.
2. Mendelev MI, Srolovitz DJ, Ackland GJ, Han S (2005) Effect of Fe segregation on the migration of a non-symmetric Sigma 5 tilt grain boundary in Al. *J Mater Res* 20(1): 208–218.
3. Falk ML, Langer JS (1998) Dynamics of viscoplastic deformation in amorphous solids. *Phys Rev E Stat Phys Plasmas Fluids Relat Interdiscip Topics* 57(6):7192–7205.
4. Honeycutt JD, Andersen HC (1987) Molecular dynamics study of melting and freezing of small Lennard-Jones clusters. *J Phys Chem* 91(19):4950–4963.
5. Tsuzuki H, Branicio PS, Rino JP (2007) Structural characterization of deformed crystals by analysis of common atomic neighborhood. *Comput Phys Commun* 177(6):518–523.

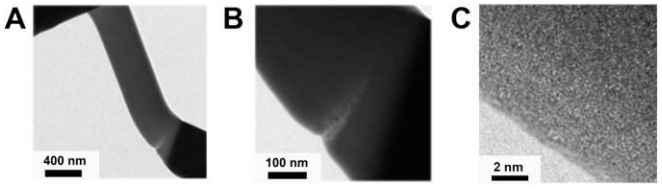

Fig. S1. The morphology of an Al-Fe metallic glass cantilever (with a total microbeam length of 2,700 nm, a middle section width of 420 nm, and a middle section thickness ~100 nm) after a monotonic bending with a displacement more than 2 μm (4.8 times the middle section width). (*A*) Extensive plastic deformation is seen in the bent specimen. (*B*) A magnified view of the highly deformed zone of the specimen where a shear band containing many nanocrystals can be seen. (*C*) High-resolution transmission electron microscope (TEM) image of the edge around the shear band after severe monotonic plastic deformation, indicating a smooth surface at the nanometer scale.

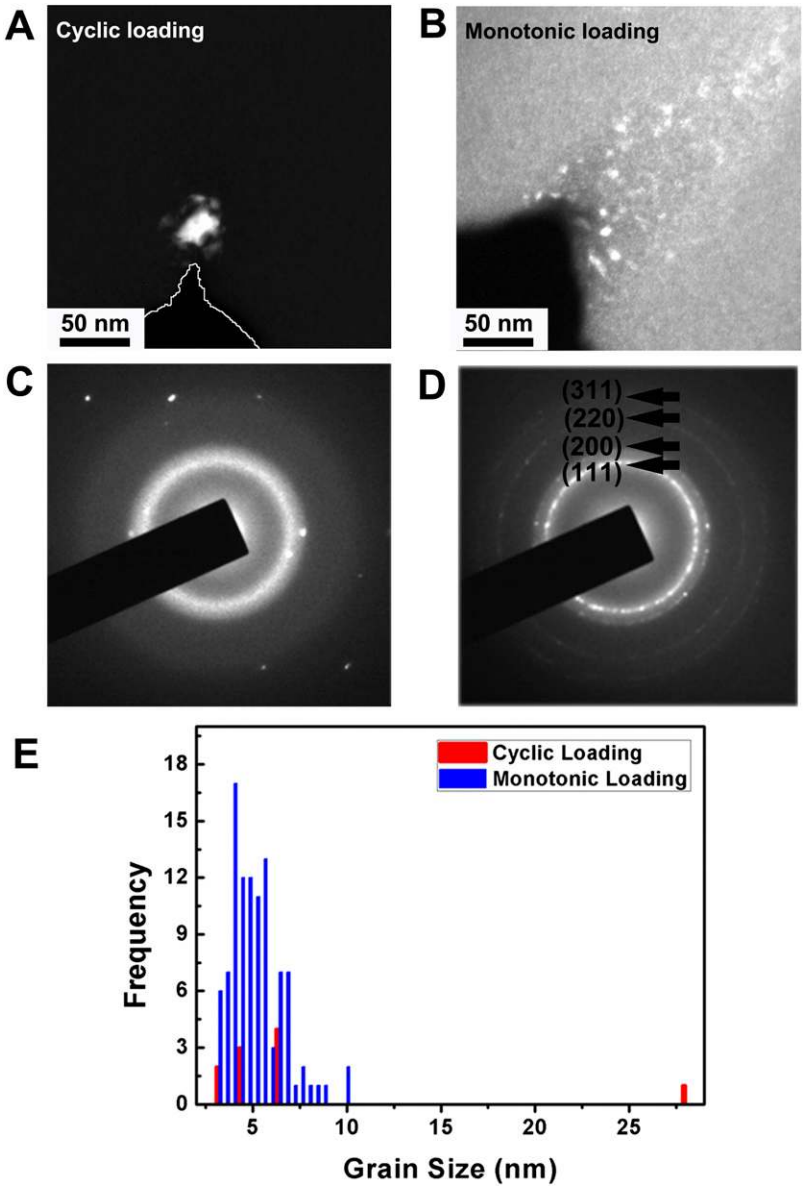

Fig. S2. Glass-to-crystal transition during cyclic and monotonic loading of metallic glass. (*A*) A large grain (~27 nm in size) with several tiny satellite grains found ahead of the fatigue crack tip after 1,500 cycles. In contrast, numerous grains smaller than 10 nm in size appeared following monotonic loading of a sample (with roughly the same initial dimensions as in Fig. S1) bent with a displacement of ~1.5 μm (about 3.6 times the middle section width). (*B*–*D*) Analyses (*B*) of the diffraction patterns (*C* and *D*) suggest that deformation-introduced crystals have a face-centered cubic structure. (*E*) The histogram of grain size vs. frequency measured in *A* and *B*.

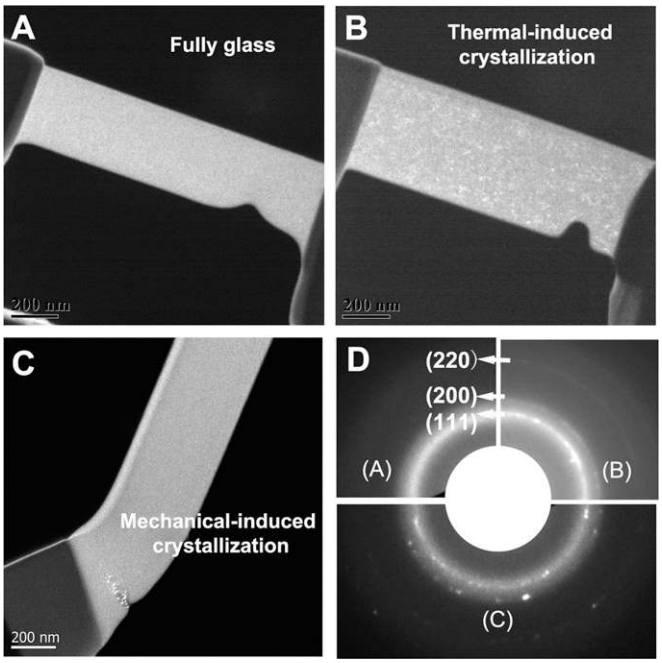

Fig. S3. Structure of mechanically induced vs. thermally induced crystal phases in Al-based metallic glass (MG) cantilevers. (*A*–*C*) Dark-field TEM images of untested, thermally treated (heated up to 150 °C for about 20 min in the air), and mechanically deformed specimens. The nanocrystals are distributed homogeneously in the specimen after thermal treatment (*B*). In contrast, crystalline phases appeared only in the plastically deformed region of the deformed specimens. (*D*) The nanocrystals, whether thermally induced or mechanically induced, all have a FCC crystal structure.

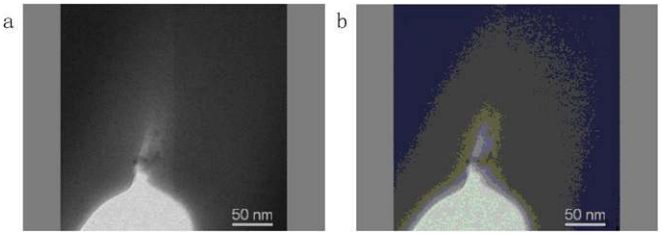

Fig. S4. (*A*) A typical original movie frame showing the notch and the crack tip. (*B*) After being converted to 8-bit from *A*.

Fig. S5. Traced notch/crack profile by applying the Sobel method.

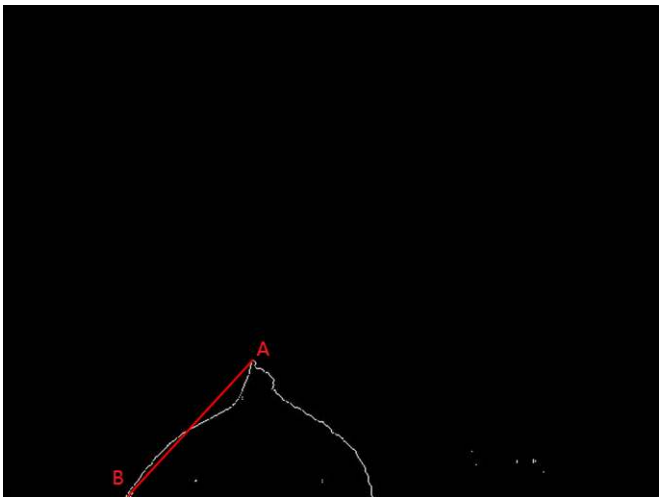

Fig. S6. Drawing a line between point A (apex of crack tip) and point B (bottom of the notch profile).

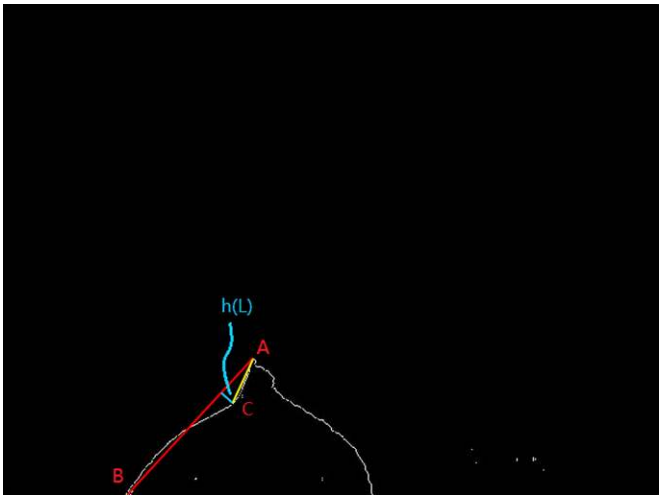

Fig. S7. Final step in extracting crack length.

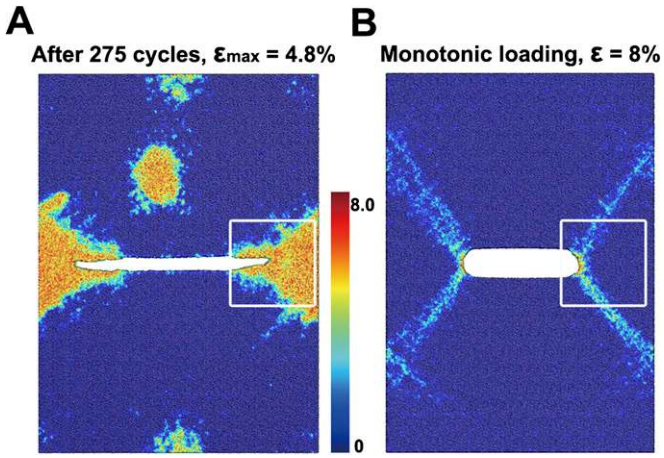

Fig. S8. MD simulations of the distribution of atomistic nonaffine displacement (D^2) in $Al_{50}Fe_{50}$ metallic glass under cyclic straining and monotonic loading. The two samples simulated were of exactly the same geometry with an internal central crack. The color bar shows the intensity scale of D^2 for both samples in units of $Å^2$. (*A*) The crack propagated quickly after 275 cycles with cyclic strain fluctuating within $3 \pm 1.8\%$. The area framed by the white box shows the active atomic nonaffine movements localized in the fatigue crack tip zone. (*B*) The sample was subjected to 8% monotonic strain that was accommodated without obvious crack propagation. The area framed by the white box indicates that the nonaffine displacement preferentially was along the maximum shear direction.

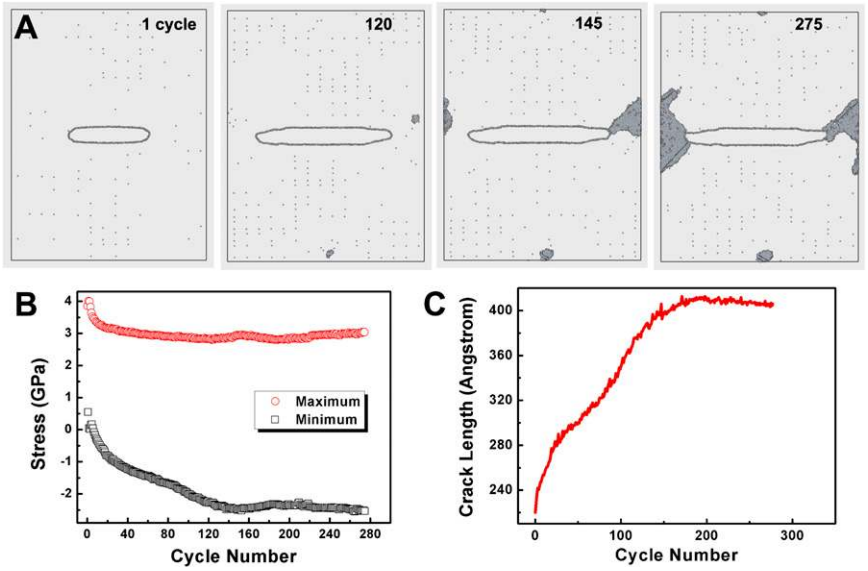

Fig. S9. MD simulation of the cycle-induced crystallization and grain growth in $Al_{50}Fe_{50}$ MG. (*A*) The atomistic configuration of coordination number [only atoms with coordinate number (CN) = 14 are visible] after different cycles (at peak strain). The crack increases rapidly without obvious crystallization for the first 110 cycles. However, a crystal phase nucleates on the right side of the fatigue crack and grows rapidly until reaching the tips of the fatigue crack. (*B*) The evolution of cyclic stress during strain cycling. (*C*) Fatigue crack length increases rapidly in the first 150 cycles, and then it begins to decrease gradually after reaching a peak. Note that the trend observed in MD is very similar to that found in our experiments (Fig. 3 in the main text).

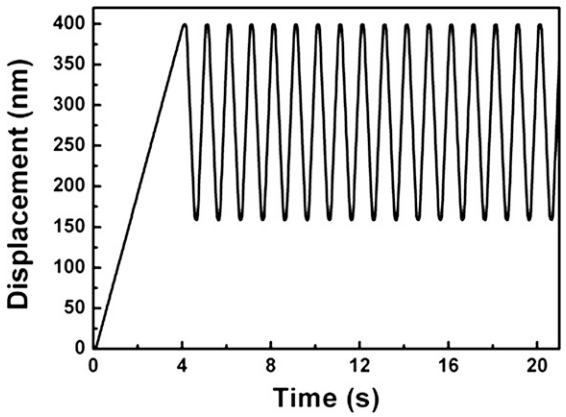

Fig. S10. Displacement-controlled cyclic straining testing with a frequency of 1 Hz and the triangular waveform used in all of the fatigue experiments reported in this work for the test geometry shown in Fig. 1*A* of the main text.

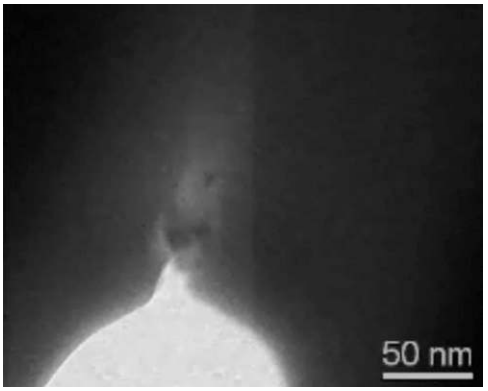

Movie S1. In situ observation of crystallization in Al-based MG beam resulting from cyclic straining inside a TEM.

Movie S1

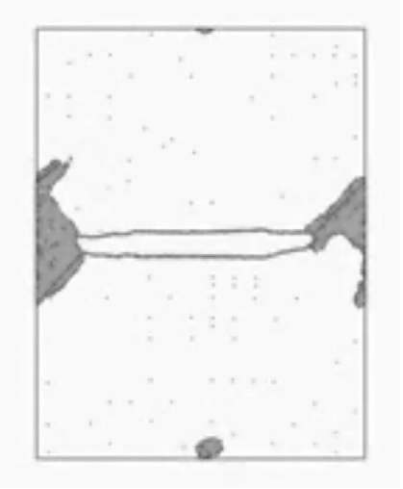

Movie S2. Atomistic configuration of the crystallization process in MG from molecular dynamics simulation.

Movie S2